sustainability

MDPI

Article

Experimental and Numerical Investigations on the Thermal Performance of Three Different Cold Plates Designed for the Electrical Vehicle Battery Module

Gökhan Sevilgen [1], Harun Dursun [1] and Muhsin Kılıç [2,*]

[1] Department of Automotive Engineering, Engineering Faculty, Bursa Uludağ University, 16059 Bursa, Türkiye; gsevilgen@uludag.edu.tr (G.S.); 511925003@ogr.uludag.edu.tr (H.D.)
[2] Department of Mechanical Engineering, Engineering Faculty, Bursa Uludağ University, 16059 Bursa, Türkiye
* Correspondence: mkilic@uludag.edu.tr

Abstract: The thermal performance of battery modules has a crucial role in the performance, safety, and lifetime of battery cells. Commonly, battery models are validated through experimental data to ensure the correctness of model behavior; however, the influences of experimental setups are often not considered in the laboratory environment, especially for prismatic cells such as lithium titanate oxide (LTO) battery cells used in electric vehicles. For this purpose, both experimental and numerical studies of the thermal performance of the battery module consisting of LTO cells was investigated using different cold plates used in electrical and hybrid vehicles. Three different discharging rates were applied to the battery module to obtain comparative results of the cooling performance. In the numerical simulations, heat generation models are typically used to observe the thermal behavior of the battery module; however, in the numerical study, dual potential multi-scale multi-domain (MSMD) battery models were used, with transient flow and heat transfer calculations performed. The numerical results were in good agreement with the experimental data. A new high-performance cold plate was developed for the thermal management of LTO battery cells. In comparison with the other two cold plate configurations, the proposed cold plate configuration dropped the maximum temperature up to 45% for the same operating conditions.

Keywords: cold plate; battery module; Li-ion; thermal performance; CFD; MSMD model

check for updates

Citation: Sevilgen, G.; Dursun, H.; Kılıç, M. Experimental and Numerical Investigations on the Thermal Performance of Three Different Cold Plates Designed for the Electrical Vehicle Battery Module. *Sustainability* **2023**, *15*, 14162. https://doi.org/10.3390/su151914162

Academic Editor: Lin Hu

Received: 28 August 2023
Revised: 22 September 2023
Accepted: 23 September 2023
Published: 25 September 2023

Copyright: © 2023 by the authors. Licensee MDPI, Basel, Switzerland. This article is an open access article distributed under the terms and conditions of the Creative Commons Attribution (CC BY) license (https://creativecommons.org/licenses/by/4.0/).

1. Introduction

Vehicles with conventional internal combustion engines threaten the health of the world due to fossil fuel consumption and harmful emissions to the environment [1]. Electric vehicles have come to the fore in the search for clean energy to address increasing environmental sensitivity, the negative effects of emission gases on human health, their effects on global climate change, periodic energy crises, and limited fossil fuel resources [2,3]. Compared to vehicles with internal combustion engines, the most important points for improvement in electric vehicles are their range and charging time [4–6]. Many studies are being carried out to improve and develop these two main points. One of the most significant parameters affecting battery performance and vehicle range is the thermal performance of the battery [7–11]. In EVs, one of the most important components is the battery package, which consists of sub-components such as cells, modules, structural elements, the battery management system (BMS) and cold plate, etc. The battery thermal management system (BTMS) is a sub-component of the BMS that plays a crucial role in increasing the efficiency of hybrid, plug-in hybrid, and also electric vehicles [12]. Moreover, efficient thermal performance leads to improved driving range and weight reduction. For instance, the use of battery package waste heat in the heating system of electric vehicles provides a driving range in electric vehicles that can be increased by up to 15% [13]. On the other hand, a non-uniform thermal distribution causes a loss of capacity and performance in the

battery; therefore, an accurate and effective cooling system is required to eliminate this non-uniform temperature distribution [14]. However, to design an effective cooling system, the thermal performance as well as the pressure drop in the cooling channels must be taken into consideration [15–17].

In many studies on BTMSs, the optimal temperature range has been determined to be in the range of 20–40 °C, and it has been recommended that the temperature be kept in this range [18,19]. However, due to the working principles of batteries, there is a tendency to heat up due to the discharge rate during operation from ohmic resistances and entropic heat changes [20]. The increase in the operating temperatures of the batteries, together with the increasing heat generation, reduce the efficiency of the battery, and may possibly damage the cells [21–23]. In addition, heat sources that may occur during operation and disrupt the homogeneous temperature distribution are also considered important; it is critical for an efficient BTMS design that the highest temperature difference between modules not exceed 5 °C [24].

In order to ensure that a battery pack can work safely and show good charging/discharging performance when operating, it is necessary to adopt a BTMS. The BTMS can be classified in terms of power consumption, working fluid, and arrangement [25]. There are various cooling methods suggested for battery thermal management systems, including air cooling [26–31], liquid cooling [32–35], PCM (phase-change material) [36–38], heat pipes [39,40], and thermo-electric coolers [41]. Each method has advantages and disadvantages in terms of its application area [42–44]. Among the cooling methods, liquid cooling systems are classified into two different applications called as direct and indirect methods [25,43]. In direct cooling systems, the coolant has direct contact with the heat source that must be cooled [45]. The batteries are submerged in the dielectric refrigerant during direct cooling [45,46]. Despite having a straightforward design and being a very efficient cooling technique, direct cooling systems are uncommon because of potential leakage issues, poorer cell temperature uniformity, higher system pressure, and increased costs [25,43]. Meanwhile, indirect liquid cooling systems offer better performance and easier control with less customizable space occupancy in BTMS applications, despite being more complicated, heavy, and expensive [43,44].

To achieve a better design of the cooling system to be used in the Li-ion battery system, first of all, the thermal behavior of Li-ion batteries should be examined in detail [35,47]. There are many models for examining the thermal behavior of Li-ion batteries. The most common sub-models used to predict thermal behavior with the help of empirical parameters are the equivalent circuit model (ECM) [48] and the Newman, Tiedemann, Gu, and Kim (NTGK) model. The NTGK model is based on semi-experimental data [49–51]. In this model, empirical parameters for the battery's thermal behavior can be obtained with the help of curve fitting from the available experimental data.

The goal of this study was to investigate the thermal performance of a battery module consisting of LTO cells, using different cold plates usually encountered in electric and hybrid vehicles. Three different discharging rates were applied on the battery module to obtain comparative results for the temperature distribution and, as a result of this study, with the considerations given above, the novelty and the main contributions to the scientific literature of this research can be stated as follows: an multi-channel cold plate was designed and prototyped for the EV. Considering, not only cooling performance but also temperature homogeneity in the battery, a new high-performance cold plate was designed and prototyped for the thermal management of prismatic Li-Ion battery cells. The numerical method and experimental data presented in this study can be utilized in further studies to design new battery packs for electric and hybrid vehicles.

2. Materials and Methods

2.1. Description of the Battery Module and Experimental Setup

The schematic view of the experimental system, including the battery module, is shown in Figure 1. The experimental system was composed of five main components: the battery module (1), the BMS (2), the electrical load (3), the PC controller (4), and the LCD

monitor (5). In the experimental studies, the battery cell selected was a 23 Ah Li-Ion cell, which had lithium titanate (LTO) anode material. The type of Li-Ion cells used in this study had advantages such as rapid charging, low-temperature operation, long life, and a high level of safety [16,17]. The electrical load used in this study was composed of electrical resistances with an air-cooling unit that provided constant discharging current during the experiments. The electrical load provides the total discharging current of the battery module, and this value can be controlled up to 250 A.

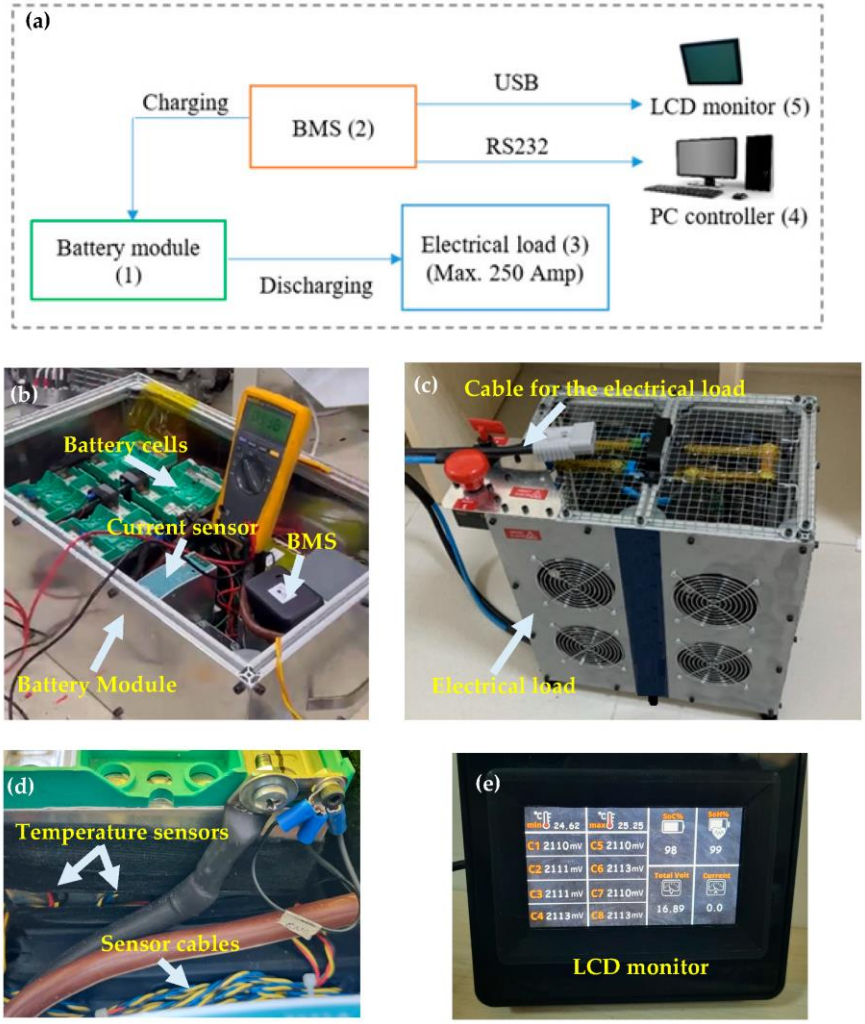


Figure 1. (**a**) The schematic diagram of the experimental system used in this study, (**b**) the battery module developed in this study, (**c**) the electrical load for the discharging process, (**d**) temperature sensors, and (**e**) LCD monitor.

A high-power LTO battery cell with a nominal capacity of 23 Ah and a nominal voltage of 2.3 V was investigated in the battery module [52,53]. This type of cell was analyzed in the European Union's Horizon 2020 Research and Innovation Program, and the researchers concluded that hybrid energy storage systems composed of both Li–S pouch cells and prismatic LTO Li-ion cells is a promising solution for optimizing the energy management of electric and hybrid vehicles [54,55].

The battery module used in the experimental study includes 16 Li-ion battery cells composed of four groups that had four cells. The two cells in the group were electrically connected in series, and both cells were connected in parallel (2S1P) in a singular group. All of the groups of battery modules were electrically connected in series (8S2P), which are shown in Figure 2.

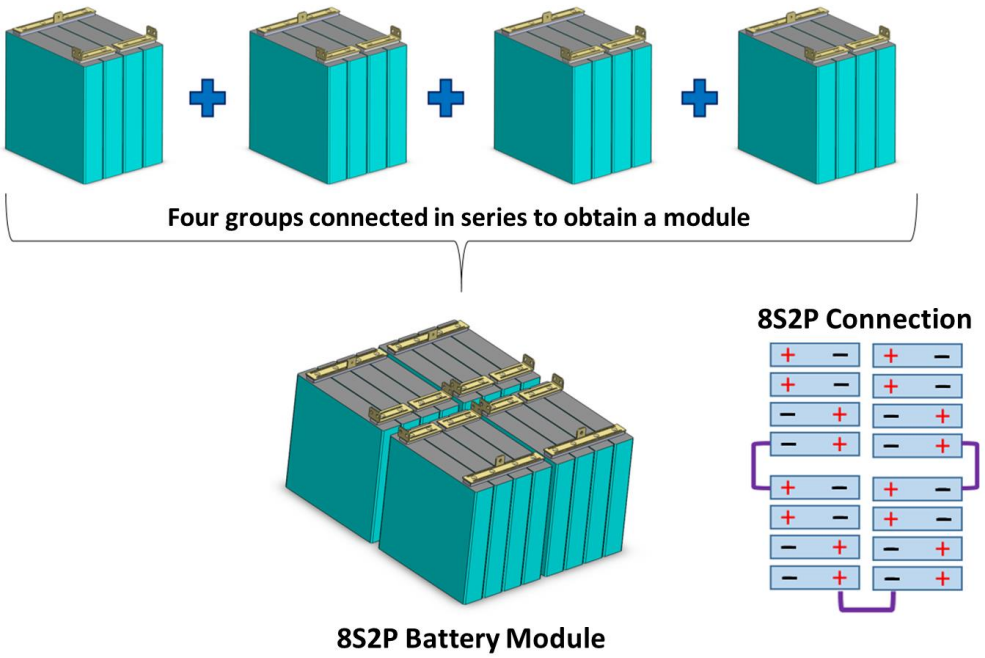


Figure 2. The electrical connection of the battery module used in the experimental study.

The characteristics of the battery module used in the experimental study are shown in Table 1. In the current study, the researchers conducted experiments using similar modules, for instance, 30 LTO cells connected in series were investigated for a hybrid thermal management system of electric vehicles [56]. The ratio of the capacity of the battery module used in this study and the physical application in real electric vehicles is about 33%. The charging process was applied to the battery module with a constant current value of 5 A, and this process took about 10 h. After the charging process, the battery module was cooled for about two hours until it reached the environmental conditions. The charging process of the module was applied once, and the discharging process was performed using an electrical load that provides the most difficult conditions instead of using cycle tests.

Table 1. The characteristics of the battery module used in the experimental study.

Properties	Li-Ion Cell
The number of cells	16
The total discharge current	46 A, 161 A, 197 A
The nominal total voltage	18.4 V
The nominal capacity	3.63 kWh
The capacity ratio	33%
The charging current and time	5 A/10 h
Cool down duration	2 h

2.2. Measurement Devices and Data Acquisition System Used in the Experimental Study

The measurement devices, which measured the ranges and accuracy of each device used in the experiments, are listed in Table 2. The temperature measurements were performed for battery cells using PT100-type temperature sensors that had different connection elements and accuracy. The locations of the measurement points and the data acquisition system used in the experiments are shown in Figures 3a and 3b, respectively. As seen in Figure 3a, there are 3 sensors on the front and back surface of the cells, where x_1 has a value of 15 mm, and y_1 and y_2 have values of 20 mm and 60 mm, respectively. Additionally, there is a temperature sensor on the side faces in the second and third cells, where the temperatures are expected to be the most intense. Thus, there are ten temperature sensors

for each group, and forty for a module. The data to be recorded from the placed sensors was used in the validation of the numerical study.

Table 2. The measurement devices accommodated in the experimental study.

Type of Device	Measuring Range	Accuracy
Internal temperature sensor	−50 °C/+400 °C	±0.01 °C
Current sensor	0–250 A	±1.0%
Temperature sensors	−25 °C/+200 °C	±0.1 °C

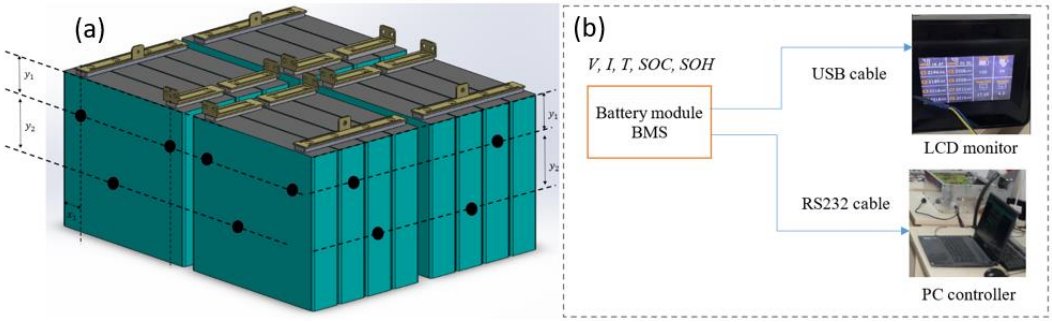


Figure 3. (**a**) The locations of temperature measurement points used in the experimental system and (**b**) the data acquisition system used in the experiments.

In order to obtain reliable temperature data, the measurement points were selected symmetrically for the front and back sides, and there was a total of six measurement points that were located on these surfaces of the battery cell. In addition, four measurement points were symmetrically chosen on the right and left side surfaces of the battery cells. Each group had ten measurement points, so the total measurement points were forty in total.

The temperature measurement data were transferred from the BMS using USB and RS232 cables. During the experiments, the BMS parameters of the battery module, such as the voltage (V), current (A), state of charge (SoC), and state of health (SoH), were monitored instantly using an LCD monitor, and recorded with a PC for the evaluation of the experimental data. The SoC of a cell denotes the capacity that is currently available as a function of the rated capacity [57]. The current mainstream SoH definition is from the capacity perspective; the SoH is defined as the ratio of the current maximum available capacity to the initial maximum capacity [58].

2.3. Theoretical Calculations and Uncertainty Analysis

In order to determine the total experimental error, uncertainty analysis was carried out using Equation (1) proposed by Moffat [59], where the Δ symbol represents the accuracy of each measurement device used for the temperature, pressure, and flow rate measurements. T, v, P, and $\dot{m}$ represent the measured temperature, velocity, pressure, and mass flow rate values during the experiments, respectively.

$$Total\ error(\%) = \left[\left(\frac{\Delta v}{v}\right)^2 + \left(\frac{\Delta T}{T}\right)^2 + \left(\frac{\Delta P}{P}\right)^2 + \left(\frac{\Delta \dot{m}}{\dot{m}}\right)^2 + \left(\frac{\Delta t}{t}\right)^2\right]^{\frac{1}{2}} \quad (1)$$

where Δt denotes the time interval of the measurement device, and t represents the total time. The highest uncertainty in experimental data was calculated to be within ±3%.

2.4. The Numerical Study

In the numerical simulations, the Ansys Fluent (Release 19.2) software package was used to simulate the transient calculations of the battery module, flow, and heat transfer simultaneously [46]. To obtain comparative results of the cooling performance with various

discharge rates, three cold plates named (i) an multi-channel cold plate, (ii) a serpentine cold plate, and (iii) bottom cold plates were designed with the help of CFD modeling, which is shown in Figure 4.

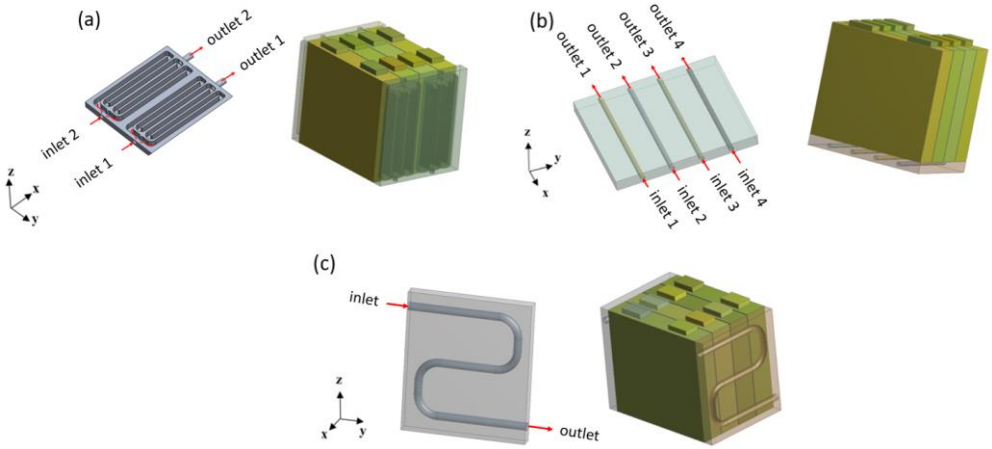


Figure 4. The CAD data of the battery group and the cooling surfaces of the (**a**) multi-channel cold plate, (**b**) bottom cold plate, and (**c**) serpentine cold plate.

The multi-channel cold plate contains parallel channels, which are advantageous in terms of the heat transfer area between the cooling fluid and solid surfaces. Therefore, better cooling performance can be achieved with a reasonable pressure drop under the same operating conditions. The multi-channel cold plate has two inlets and two outlets, while the serpentine plate has only a single inlet and outlet surface. The third, the one bottom cold plate, has four inlet and outlet surfaces, which are provided by four tubes. The cooling performance of the multi-channel cold plate was compared with the conventional serpentine plate and the bottom cold plate currently used in applications of electric vehicle battery cooling units with the help of CFD. All of the cooling plates were analyzed in such a way that the mass flow rates were equal in the main inlet section, and this value was chosen to be 0.01 kg/s.

The mesh structure of the battery module, all of the cold plates used in the numerical model, and the computational domain for the module used in this study are shown in Figure 5. Due to the symmetrical properties of the battery module used in this study, a battery group with four cells including the cold plates was used in the numerical calculations to reduce the computational time and quickly evaluate the thermal performance of the different cold plates. The mesh domain of the computational domain was very important for obtaining accurately predicted results and reducing the computing time in the numerical calculations [13–15]. In the numerical calculations for incompressible flow with constant properties, the continuity, momentum, and energy equations for transient conditions of water flow can be written using Equations (2)–(8) in scalar form, where u, v, and w are the velocity components, ∂p is the pressure drop, v is the kinematic viscosity (m^2/s), T is the temperature (K), ρ is the density (kg/m^3), k is the thermal conductivity (W/mK), c_p is the specific heat of fluid (J/kg K) in the computational domain, and g is the acceleration of gravity (m/s^2).

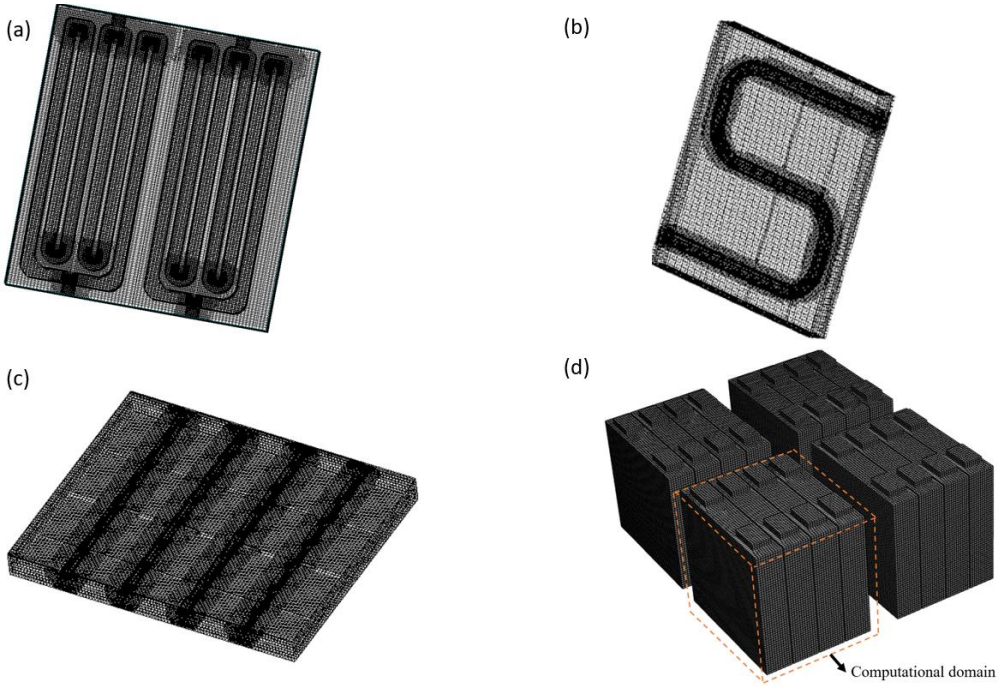


Figure 5. The mesh structure of (**a**) multi-channel cold plate, (**b**) serpentine plate, (**c**) bottom cold plate, and (**d**) the module consists of 16 battery cells and the computational domain.

The continuity equation for the fluid domain can be written as follows:

$$\frac{\partial(\rho u)}{\partial x} + \frac{\partial(\rho v)}{\partial y} + \frac{\partial(\rho w)}{\partial z} = 0 \tag{2}$$

The momentum conservation equations in the x, y, and z directions are respectively shown as follows:

$$\frac{\partial u}{\partial t} + u\frac{\partial u}{\partial x} + v\frac{\partial u}{\partial y} + w\frac{\partial u}{\partial z} = -\frac{1}{\rho}\frac{\partial p}{\partial x} + \nu\left(\frac{d^2u}{dx^2} + \frac{d^2u}{dy^2} + \frac{d^2u}{dz^2}\right) \tag{3}$$

$$\frac{\partial v}{\partial t} + u\frac{\partial v}{\partial x} + v\frac{\partial v}{\partial y} + w\frac{\partial v}{\partial z} = -\frac{1}{\rho}\frac{\partial p}{\partial x} + \nu\left(\frac{d^2v}{dx^2} + \frac{d^2v}{dy^2} + \frac{d^2v}{dz^2}\right) \tag{4}$$

$$\frac{\partial w}{\partial t} + u\frac{\partial w}{\partial x} + v\frac{\partial w}{\partial y} + w\frac{\partial w}{\partial z} = -\frac{1}{\rho}\frac{\partial p}{\partial x} + \nu\left(\frac{d^2w}{dx^2} + \frac{d^2w}{dy^2} + \frac{d^2w}{dz^2}\right) + \rho g_z \tag{5}$$

The energy equation for the fluid domain, can be written using Equation (6) for the fluid zone with transient conditions, where Φ is the dissipation function that can be calculated from Equation (7). For the solid zones, the energy equation can be written in Equation (8), where, S is the source term that includes volumetric heat generation; k_s is the thermal conductivity, ρ_s is the density, and $c_{p,s}$ is the specific heat of the solid materials used in this study.

$$\rho c_p\left(\frac{\partial T}{\partial t} + u\frac{\partial T}{\partial x} + v\frac{\partial T}{\partial y} + w\frac{\partial T}{\partial z}\right) = k\,\nabla^2\mathrm{T} + \Phi \tag{6}$$

$$\Phi = \mu\left[2\left[\left(\frac{\partial u}{\partial x}\right)^2 + \left(\frac{\partial v}{\partial y}\right)^2 + \left(\frac{\partial w}{\partial z}\right)^2\right] + \left(\frac{\partial v}{\partial x} + \frac{\partial u}{\partial y}\right)^2 + \left(\frac{\partial w}{\partial y} + \frac{\partial v}{\partial z}\right)^2 + \left(\frac{\partial u}{\partial z} + \frac{\partial w}{\partial x}\right)^2\right] \tag{7}$$

$$\frac{\partial}{\partial x}\left(k_s\frac{\partial T}{dx}\right) + \frac{\partial}{\partial y}\left(k_s\frac{\partial T}{dy}\right) + \frac{\partial}{\partial z}\left(k_s\frac{\partial T}{dz}\right) + S = \rho_s c_{p,s}\frac{\partial T}{\partial t} \tag{8}$$

For the numerical analysis, the SIMPLE algorithm was chosen for pressure–velocity coupling, the numerical calculations were performed with unsteady conditions, and convergence was assumed when the normalized residuals of the flow equations were less than 10^{-3} and the energy equation was less than 10^{-6}. No slip boundary condition was used for solid–fluid boundary surfaces, and the ambient air temperature was assumed to be a constant value of 290.5 K, considering the experimental conditions. For the battery module, the NTGK sub-model was used for modeling each battery cell's characteristics in the module. The boundary conditions used in the numerical calculations are listed in Table 3.

Table 3. Boundary conditions used in the numerical simulation.

Surfaces or Domains	Boundary Conditions
Supply temperature of coolant	Constant temperature value of 290.5 K
Outlet surface of cooling block	Gauge pressure equals to 0 Pa
Mass flow rate of coolant at the main inlet section	0.01 kg/s
Battery module with 16 cells	NTGK model
Outer surfaces of solid domains contact with air	Free convection boundary condition
Flow conditions	Laminar flow with unsteady conditions
Ambient temperature	293 K
Material Type	**Solid Domains**
Multi-channel cold plate	Aluminum
Serpentine channel	Copper tube with aluminum cold plate
Bottom cold plate	Copper tube with aluminum cold plate
Outer surfaces of all cold plates	Convection boundary condition

Three different cold plates were used in the numerical calculations. The second and third plates were serpentine and bottom cold plates, which are usually used for cooling applications of battery packs in electric vehicles. The first one was developed in this study to achieve better results in the thermal performance of battery cooling, in which the water flow separates into two parallel flow regions, in order to obtain a homogenous temperature distribution on the battery module surfaces.

For the outer surfaces of solid zones in contact with ambient air, the free convection condition was used. In the numerical calculations, at the inlet region of all of the cooling blocks, the mass flow rate of coolant was selected to be a constant value of 0.01 kg/s to obtain comparative results with the same conditions.

Two main methods are used to predict the progress of chemical, electrical, and thermal processes in a battery: (1) the single potential empirical battery model (SPEBM), and (2) the dual potential multi-scale multi-domain (MSMD) battery model. The single potential empirical battery model is useful for electrode scale estimates in a single battery cell. However, as in this study, it is not be very efficient to use this model to study all of the complex electrochemical events in and large-scale geometry systems [14]. Compared to the SPEBM, the MSMD battery model solves these limitations using a homogeneous model of a multi-scale multidimensional approach [60]. Three electrochemical sub-models can be applied to various investigations, (1) the Newman, Tiedemann, Gu, and Kim (NTGK) empirical model, (2) the equivalent circuit model (ECM), and (3) the Newman subs pseudo 2D (P2D) model complexity level. These sub-models have been useful in terms of their flexibility in the study of physical and electrochemical phenomena with various length scales [61].

In this study, the NTGK model was chosen to simulate the transient behavior of the battery module, since it requires fewer parameters, is suitable for larger length scales, and is a semi-empirical model where data from the existing battery module system can be used. Selecting the NTGK model and using the data obtained from the experiments with the battery system increased the reliability of the simulation model, and facilitated the validation studies.

In the NTGK model, the electrical and thermal field properties of the battery are formulated as given in Equations (9)–(11) in the cell-scale computational space of the battery [62]:

$$\frac{\partial \rho C_p T}{\partial t} - \nabla \cdot (k_C \nabla T) = \sigma_{pos} \mid \nabla \varphi_{pos} \mid^2 + \sigma_{neg} \mid \nabla \varphi_{neg} \mid^2 + q_{ech} \quad (9)$$

$$\nabla \cdot (\sigma_{pos} \nabla \varphi_{pos}) = -j$$

$$\nabla \cdot (\sigma_{neg} \nabla \varphi_{neg}) = j \quad (10)$$

where σ is the electric conductivity, φ is the electric potential, and subscripts *pos* and *neg* refer to positive and negative electrodes, respectively. The volumetric current transfer rate formula is written in Equation (11) [63], as follows:

$$j = \frac{C_N}{C_{ref} Vol} Y \left[U - (\varphi_{pos} - \varphi_{neg}) \right] \quad (11)$$

where *Vol* is the volume of the active zone, C_{ref} is the capacity of the battery used to achieve the U and Y function parameters by the parameter estimation tool in Fluent via the discharging results. According to the deep of discharge (DOD), the U and Y functions are calculated as shown in Equations (12) and (13), respectively [64]:

$$U = \left(\sum_{n=0}^{5} a_n (\mathrm{DOD})^n \right) - C_2 \left(T - T_{ref} \right) \quad (12)$$

$$Y = \left(\sum_{n=0}^{5} b_n (\mathrm{DOD})^n \right) \exp \left[-C_1 \left(\frac{1}{T} - \frac{1}{T_{ref}} \right) \right] \quad (13)$$

where T_{ref} is the reference temperature, and C_1 and C_2 are constant values for the particular battery. In Equation (14), the heat of the electrochemical reaction, q_{ech}, is given as follows [64]:

$$q_{ech} = j \left[U - (\varphi_{pos} - \varphi_{neg}) - T \frac{dU}{dT} \right] \quad (14)$$

where the first term represents the heat due to the over potential, and the second term is the entropic heat generation. The detailed properties of the materials for the NTGK model are shown in Table 4.

Table 4. Material properties for the MSMD model.

Properties	Aluminum (Positive Tab)	Steel (Negative Tab)	Jelly Roll (Active Zone)
Density (kg/m^3)	2719	8030.0	2226
Specific heat (J/kg-K)	871	502.48	1197
Thermal conductivity (W/mK)	202.4	16.27	27
Electrical conductivity (S/m)	3.541×10^7	8.33×10^6	1.19×10^6, 9.83×10^5

A battery module system consisting of 16 cells with a nominal cell voltage of 2.3 V and electrically connected as 8S2P was used for the present study. There was a battery management system present, in order to safely measure and manage the voltage, current, and temperatures of the battery system during charging and discharging. Moreover, there was a flexible resistance system to apply different discharge rates in the battery system. Experiments were made with this resistance system using 16 cells of the battery system with discharge rates of 1 C (46 A), 3.5 C (161 A), and approximately 4.25 C (197 A). The experiments were carried out at a controlled ambient temperature of 17.5 °C, and without any additional cooling or heating systems. During the experiments, an RS232 connection was used to record the data, and the voltage, current, and temperature values were focused.

The temperature data were obtained with the help of forty PT100 temperature sensors placed in specific locations of the cells in the battery module, and other data were recorded directly from the BMS. The charging process was achieved using an internal charging device in the battery module. After conducting the charging process once, the discharging process was applied using an electrical load that provides the most difficult conditions instead of using cycle tests.

The data obtained from the experimental study mentioned in this section were used as input, while creating the MSMD simulation module. After performing the experiments, the same conditions were created in the CFD study, and simulations were carried out. In the simulation model, the ambient temperature and the initial temperature were taken as 290.5 K, and the characteristics of the battery system were defined with the parameter estimation tool (PET) in the MSMD battery model.

3. Results and Discussion

3.1. Comparisons of Experimental and Numerical Results

Validation of the numerical results was achieved by comparing the experimental results of the voltage and temperature characteristics with different discharge rates. At first, the voltage characteristics were compared to the experimental data, and then the comparative temperature results of numerical simulation and experimental data were obtained. In the validation study, the battery module with the 8S2P electrical connection was used in both the experimental study and the numerical study. In the experiments and simulations, the voltage values were taken as the average voltage of the 16 cells. Additionally, the temperature data obtained from 40 different locations were collected, and their average values were taken for evaluation of the thermal behavior of the battery module.

As seen in the voltage–time graph in Figure 6, the simulation results represent the voltage characteristic like the experiments. It starts from approximately 2.60 V and ends at approximately 1.50 V, which is the stopping criterion. In addition, the voltage-decreasing speed is compatible with that of the experiments and the catalog values. The experimental results show that the voltage values start from approximately 2.60 V and reach nearly 1.65 V. According to the cell catalog values, the voltage value should drop to 1.50 V, but since it is difficult to obtain the data in the fast voltage drop region, data decreasing to 1.65 V can be recorded. The reason for the data terminating after this value is that the battery management system drops the minimum voltage value, and stops the battery system to protect the cells.

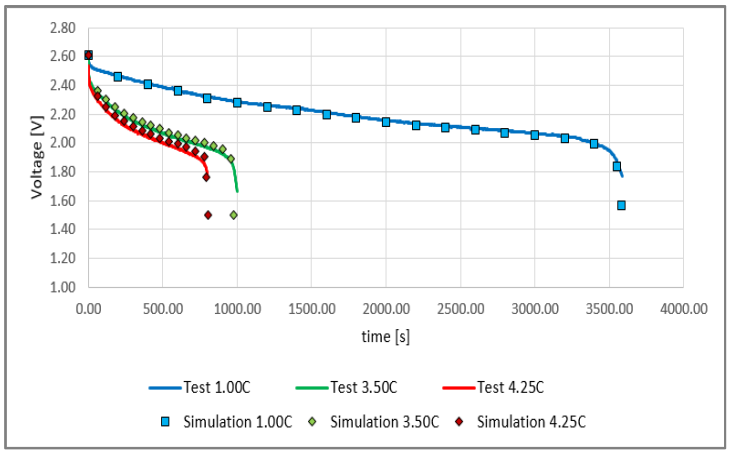


Figure 6. Voltage–time graph comparison of the experiments and simulations with the battery module at three different discharge rates.

Battery cells are complex electrochemical and thermodynamic systems, and multiple factors impact battery performance. Battery discharge curves are based on battery polariza-

tion that occurs during discharge. During discharge, batteries experience a drop in voltage. The drop in voltage is related to several factors, such as ohmic polarization, activation polarization, and concentration polarization. Ohmic polarization is caused by the battery's internal resistance; activation polarization depends on electrochemical reactions; and concentration polarization is the resistance faced by the mass transfer (diffusion) process by which ions are transported across the electrolyte from one electrode to another [65,66].

The data obtained from the experimental results are compatible with the catalog voltage characteristic of the cells. According to the results, it is obvious that the battery voltage characteristic defined with the help of a parameter estimation tool (PET) and the voltage graph obtained as a result of the experiments almost overlap. Only minor differences occur in the last part of the graph, where there is a high voltage drop.

Figure 7 shows the graphs of the average temperature data recorded at three different discharge rates. In the average temperature–time graph of the simulations with three different discharge rates, the results of the average temperature values obtained in the simulation study, depending on time, are seen. As a result of the simulation, the temperature increased by approximately 5 K, at a discharge rate of 1.00 C. Meanwhile, the temperature rise value for 3.50 C is around 19.50 K; for 4.25 C, the increased temperature value is nearly 24 K. Similar to the experimental results, it was determined that the temperature increase value increased as the discharge rate increased. In the average temperature–time graph of the experiment for the 1.00 C discharge rate, the temperature increases by nearly 6 K, while for 3.50 C, the temperature rise is approximately 22.5 K for the 1 C discharge rate. When the highest discharge rate of 4.25 C was applied, a temperature increase of approximately 26 K was observed. These results show that as the discharge rate increases, the temperature change accelerates.

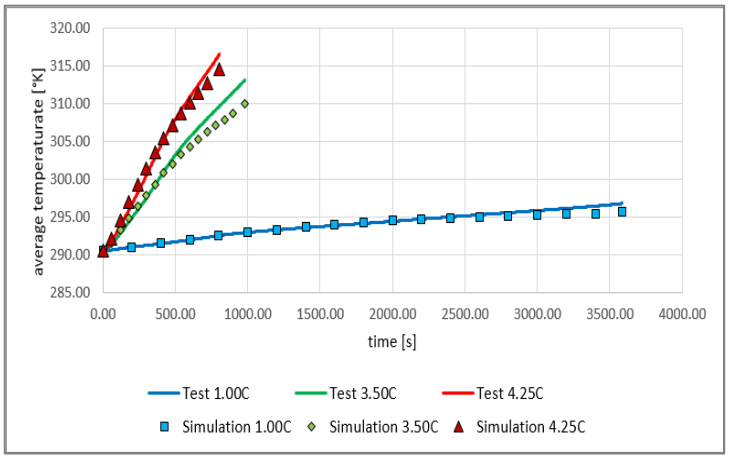


Figure 7. Average temperature–time graph comparison of the experiments and simulations with the battery module at three different discharge rates.

There is a great similarity between the experimental results and simulation results at 1.00 C. There is a deviation of about 1 K from the maximum temperature value. At the 3.50 C discharge value, increasing deviations were observed between the experimental and simulation results over time. This deviation value remains around 3 K maximum. At the 4.25 C discharge rate, there is a similar situation to 3.50 C. At the 4.25 C discharge rate, the maximum deviation from the average temperature values is around 2 K.

According to all of the results above, it can be easily stated that the experimental results and the simulation results greatly overlap with each other, due to the fact that the maximum deviations are at reasonable levels, although the deviations in temperatures increased over time at high discharge rates. Therefore, the established simulation model can be considered to represent the operating conditions and characteristics of the current battery system.

3.2. Mesh Independency Analysis

The calculated maximum temperature of the battery module was selected for mesh independency analysis because the temperature gradients varied significantly on the surface temperature of battery cells, depending on the value of the discharging current. In the mesh dependency analyses, the discharging rate was selected as a maximum value of 4.25 C, due to calculated higher temperature gradients for this case. The numerical results of the mesh independency analysis are shown in Figure 8. From these results of the mesh independency analysis, it was found that about one million elements in total were enough for the temperature predictions.

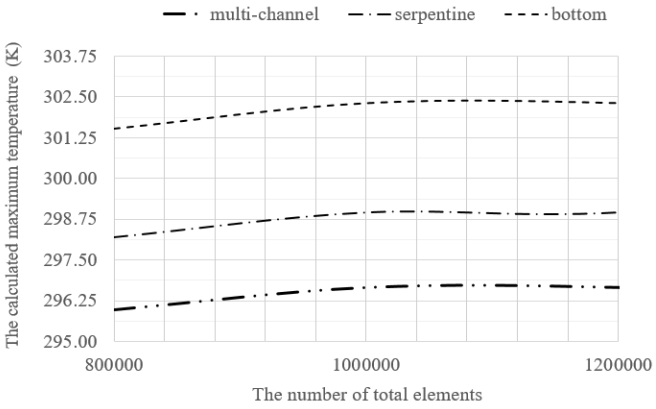


Figure 8. The numerical results of mesh independency analysis.

3.3. Numerical Analysis Results and Discussion

The temperature starts to increase from the top of the cells from the beginning of the simulation study for the battery module without cooling, as seen in Figure 9. Then, the temperature distribution descends to the middle of the cell, and proceeds to the middle of the surface of the battery cell; the highest temperature is obtained in the middle of the battery cell. The temperature decreases in gradients from the middle of the battery cell to the outside of the cell surface.

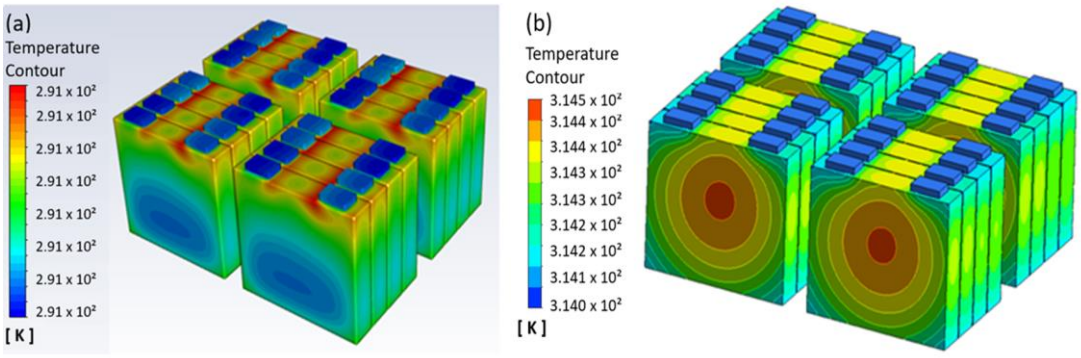


Figure 9. The temperature distribution of battery module without cooling for 4.25 C; (**a**) t = 15 s; (**b**) t = 840 s.

In temperature gradients at all discharge rates for each cooling unit, the temperature gradients that emerged as a result of the simulation study performed at 1 C, 3.5 C, and 4.25 C discharge rates of all of the cooling units are seen in Figure 10. According to the temperature gradients of the cold plate, serpentine plate, and cooling pipes, it can easily be observed that the cold plate affects the temperature of battery cells over a wider area.

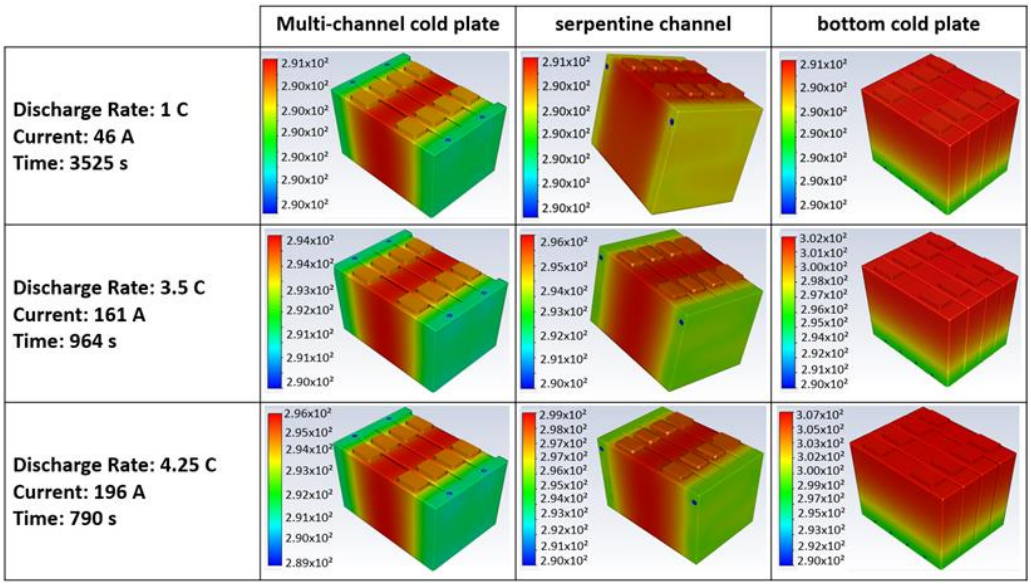


Figure 10. Temperature gradients at all discharge rates for each cooling unit.

According to the graphs in Figure 11, where the average temperatures at the 1 C discharge rate are given, it was observed that the temperatures decreased for a short time in the first operation, increased after a while, and then decreased again after reaching thermal equilibrium. Meanwhile, the maximum average temperature in the bottom cold plate exceeded 291.2 K, and it exceeded 290.60 K in serpentine plate cooling. On the other hand, in multi-channel cold plate cooling, the average temperature never reached 290.5 K after the starting condition.

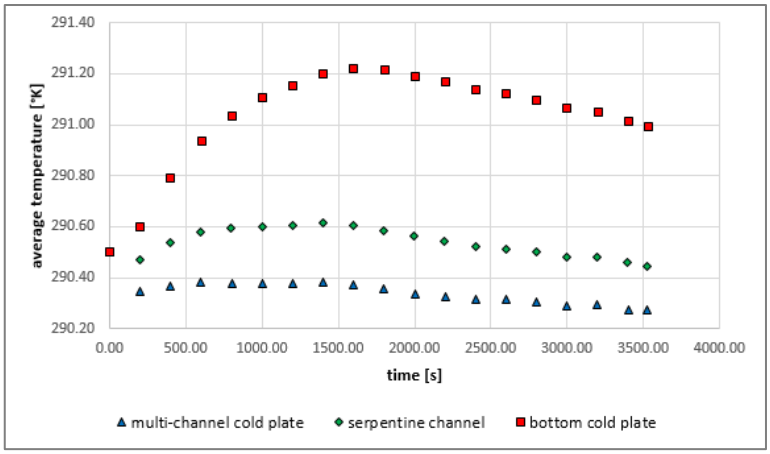


Figure 11. Comparison of average temperature of cooling units at 1 C discharge rate.

In the simulation graphics performed with a discharge rate of 3.50 C shown in Figure 12, the average temperature in all of the cooling units increases for a while, but after a reasonable time, it reaches equilibrium and the temperature increase stops. The maximum average temperatures reached for the bottom cold plate, serpentine plate, and multi-channel cold plate are 300 K, 296 K, and 294 K, respectively. The average temperature values obtained as a result of the simulation show that the cooling by the multi-channel cold plate provided an approximately 2 K lower temperature than the serpentine plate, and an almost 6.5 K lower temperature than the bottom cold plate.

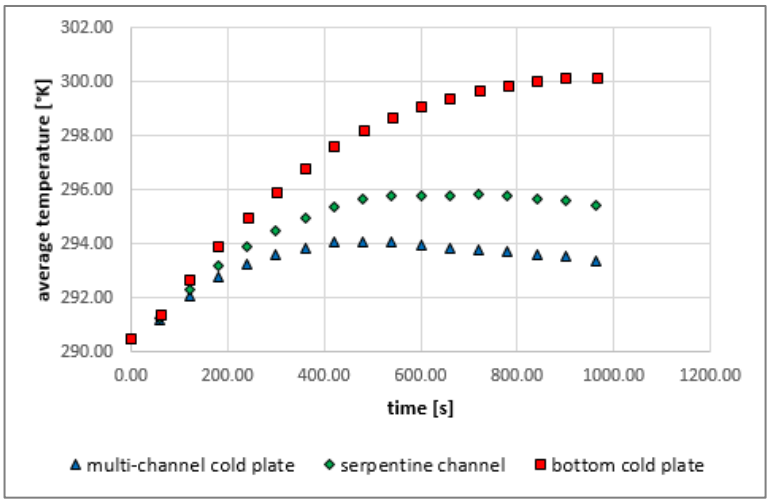


Figure 12. Comparison of average temperature of cooling units at 3.50 C discharge rate.

The average temperature values at the 4.25 C discharge rate, as seen in Figure 13, show a temperature change characteristic that is similar to the results obtained at the 3.50 C discharge rate. As with the low discharge rate, the maximum average temperature obtained at the high discharge rate was also achieved by the bottom cold plate, and is around 304 K. For the serpentine plate, the average temperature is 2.5 K higher than the discharge rate for 3.50 C, while the temperature increase for the multi-channel cold plate cooling is around 1.7 K.

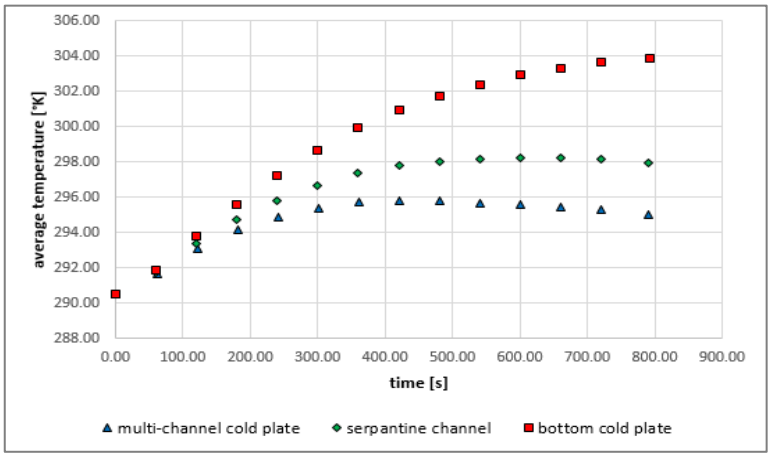


Figure 13. Comparison of average temperature of cooling units at 4.25 C discharge rate.

According to the average temperature data shown in Table 5, all of the cooling units showed an effective performance for the 1 C discharge rate, and the temperature increase was prevented. For a discharge rate of 3.50 C, the multi-channel cold plate was able to decrease the average temperature by approximately 16 K, while the serpentine plate was able to decrease it by 14 K. In the case of cooling with the bottom cold plate, a temperature decrease of approximately 9.50 K was observed. Considering the performance of all of the cooling units at a discharge rate of 3.50 C, the multi-channel cold plate showed the best performance. The worst cooling performance was realized in the bottom cold plate method.

At a discharge rate of 4.25 C, the multi-channel cold plate achieved around 19 K of cooling, while the serpentine plate cooled nearly 16 K and was able to maintain a temperature of around 298 K. For the bottom cold plate method, the temperature exceeded 300 K and was kept at around 304 K. This means that it provided a cooling of approximately 10.50 K.

Table 5. Calculated average temperature and temperature drop values in the battery pack.

	Discharge Rate	Average Temperature (K)	Maximum Temperature (K)	Average Temperature Decrease (K)
Without cooling	1.00 C	295.70	297.12	-
	3.50 C	309.89	313.23	-
	4.25 C	314.57	321.53	-
Multi-channel cold plate	1.00 C	290.44	291.12	5.26
	3.50 C	293.60	294.81	16.29
	4.25 C	295.27	296.23	19.30
Serpentine cold plate	1.00 C	290.60	291.34	5.10
	3.50 C	295.70	296.91	14.19
	4.25 C	298.20	299.31	16.37
Bottom cold plate	1.00 C	291.19	291.87	4.51
	3.50 C	300.41	302.22	9.48
	4.25 C	304.09	309.28	10.48

The calculated average heat transfer coefficients for all of the cold plates are provided in Table 6. It can be seen that the convective heat transfer coefficient varied from 517 W/m^2K to 1358 W/m^2K, and the highest heat transfer coefficient was obtained for the bottom cold plate. Meanwhile, the highest total convective heat transfer area was achieved with the multi-channel cold plate. The calculated convection heat transfer resistance values are 0.073, 0.0822, and 0.162 for the multi-channel, serpentine, and bottom cold plates, respectively. These results reveal that the multi-channel cold plate rejects more heat under the same operating conditions. Therefore, it shows better cooling performance compared to the others.

Table 6. Calculated average heat transfer coefficient and convection resistance values.

Heat Transfer Characteristics	Multi-Channel Cold Plate	Serpentine	Bottom
Total convective heat transfer area (m^2)	0.0265	0.0108	0.00455
Average heat transfer coefficient (W/m^2K)	517	1130	1358
Convection heat transfer resistance (K/W)	0.0730	0.0822	0.162

The calculated maximum temperature differences obtained at the surfaces of battery cells in the module are shown in Figure 14. From these results, the multi-channel and serpentine cold plates had nearly similar calculated temperature differences, and these values ranged from 3 K to 4 K. Thus, they present more homogeneous temperature distributions in the battery modules. However, for the bottom cold plate, higher temperature differences were obtained, a value of 8 K under a 4.25 C discharging current.

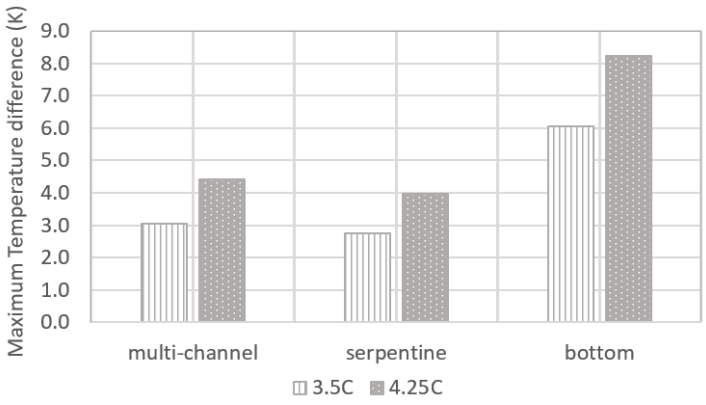


Figure 14. Comparison of the calculated maximum temperature differences obtained for three different cold plates at the end of the numerical simulations.

The calculated total pressure drops for different mass flow rates are shown in Figure 15. From the results, we can easily state that the serpentine and multi-channel cold plates had almost similar values; however, the bottom cold plate had the highest total pressure drop. As a result, it can be stated that the multi-channel cold plate provided higher cooling performance with a reasonable pressure drop compared to the serpentine cold plate, and it had advantages in terms of achieving the lowest average temperature and temperature uniformity in the battery pack.

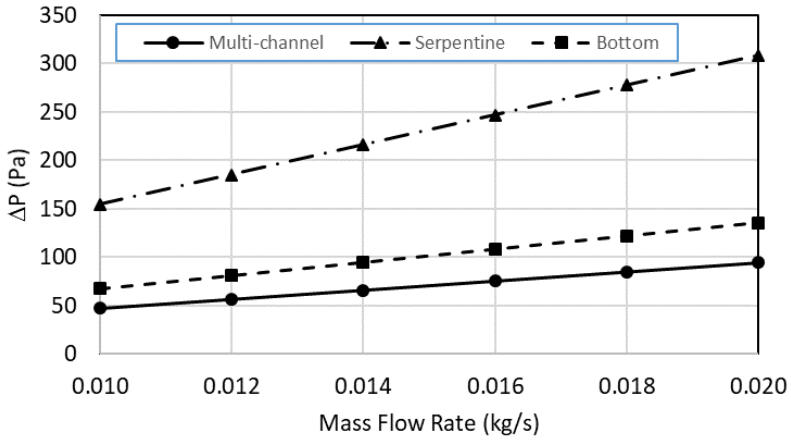


Figure 15. The calculated total pressure drop versus mass flow rate (kg/s) for different cold plates.

When the performances of the cooling units are compared across all of the discharge rates, it is clearly seen that the cooling performance of the multi-channel cold plate has the best performance. Therefore, using the multi-channel cold plate developed in this study for applications operating at high discharge rates is more effective in terms of battery life cycles and thermal efficiency.

4. Conclusions

In this research, three different cold plates were thermally compared for three different discharge rates. Experimental and numerical results were obtained considering different discharge rates for evaluating the thermal performance of the battery modules with liquid cooling plates.

Considering the temperature values obtained at different discharge rates, it is obvious that the newly designed cold plate is thermally more effective than the other conventional designs. In terms of the temperature difference at different locations of the battery module, the multi-channel cold plate had more homogeneity for the higher discharge rate compared to the other cold plate designs. As a result, the multi-channel cold plate is more suitable for high-power applications of a battery module. The thermal management of battery modules has a great effect on the life cycle and vehicle driving range of battery packs for electric vehicles, so it provides sustainable technology for the automotive industry, achieving battery package recycling targets and also improving energy efficiency.

From the numerical results of the serpentine cold plate, we can easily state that it is suitable for applications that require moderate electrical power. The bottom cold plate had lower performance compared to the multi-channel and serpentine cold plates, and it also had a heterogeneous temperature distribution. Therefore, the bottom cold plate design is not be effective enough for applications that require moderate or high electrical power.

The multi-channel and serpentine cold plates had very similar calculated maximum temperature differences, and these values ranged from 3 K to 4 K. However, for the bottom cold plate, higher temperature differences were obtained, a value of 8 K, under the 4.25 C discharging current. On the other hand, it can be stated that the multi-channel cold plate provided better cooling performance with a reasonable pressure drop compared to the serpentine cold plate, and it also had advantages in terms of achieving temperature uniformity.

A detailed numerical and experimental analysis was performed to obtain a thermal comparison among the liquid cold plates, utilizing different discharge rates of the battery module. With the considerations given above, the conclusions can be stated as follows:

1. A new higher-performance cold plate that has parallel water flow channels was designed for the thermal management of prismatic Li-ion battery cells in the present study.
2. Using the multi-channel cold plate developed in this study, the temperature was reduced dramatically for higher discharging rates.
3. A three-dimensional electro–thermal model that included flow and heat transfer analysis under transient conditions was developed for the evaluation of the thermal performance of three different liquid cold plates.
4. The numerical simulation results were in good agreement with the experimental data so that for the battery module with the NTGK sub-model, flow and heat transfer analyses in transient numerical calculations were performed simultaneously for the cooling performance, apart from the heat generation models described in the literature.
5. The results of this study contribute to the experimental setups considered in the laboratory environment, especially for prismatic cells such as LTO battery cells used in electric vehicles.
6. Considering the cooling performance and temperature homogeneity, a new higher-performance cold plate was designed for the thermal management of prismatic Li-ion battery cells.

In future studies, the thermal performance of the battery pack will be investigated with the validated model of the battery module, with a focus on the effect of driving cycles, fast charging, and ambient conditions on the cooling performance of liquid cold plates.

Author Contributions: Conceptualization, G.S. and M.K.; methodology, G.S., M.K. and H.D.; software, G.S. and M.K.; validation, G.S. and H.D.; formal analysis, G.S., M.K. and H.D.; investigation, G.S., M.K. and H.D.; resources, G.S., M.K. and H.D.; data curation, G.S., M.K. and H.D.; writing—original draft preparation, G.S. and H.D.; writing—review and editing, G.S. and M.K.; supervision, M.K. and G.S.; project administration, G.S.; funding acquisition, G.S. and H.D. All authors have read and agreed to the published version of the manuscript.

Funding: This research was funded by TÜBİTAK, funding numbers are 219M475 and 22AG001.

Institutional Review Board Statement: Not applicable.

Informed Consent Statement: Not applicable.

Data Availability Statement: Not applicable.

Acknowledgments: The authors wish to thank the Scientific and Technological Research Council of Turkey (TUBITAK) for supporting this research under the projects numbered 219M475-TÜBİTAK 1001 and 22AG001-TÜBİTAK 1004, and the authors gratefully acknowledge the Li-Ion battery cells provided by Altınay Electromobility and Energy Technologies Inc., Bursa, Türkiye.

Conflicts of Interest: The authors declare no conflict of interest.

References

1. Bach, W. Fossil Fuel Resources and Their Impacts on Environment and Climate. *Int. J. Hydrogen Energy* **1981**, *6*, 185–201. [CrossRef]
2. Querini, F.; Dagostino, S.; Morel, S.; Rousseaux, P. Greenhouse Gas Emissions of Electric Vehicles Associated with Wind and Photovoltaic Electricity. *Energy Procedia* **2012**, *20*, 391–401. [CrossRef]
3. Zhao, G.; Baker, J. Effects on Environmental Impacts of Introducing Electric Vehicle Batteries as Storage—A Case Study of the United Kingdom. *Energy Strategy Rev.* **2022**, *40*, 100819. [CrossRef]
4. Miwa, T.; Sato, H.; Morikawa, T. Range and Battery Depletion Concerns with Electric Vehicles. *J. Adv. Transp.* **2017**, *2017*, 7491234. [CrossRef]
5. Kostopoulos, E.D.; Spyropoulos, G.C.; Kaldellis, J.K. Real-World Study for the Optimal Charging of Electric Vehicles. *Energy Rep.* **2020**, *6*, 418–426. [CrossRef]
6. Chakraborty, P.; Parker, R.; Hoque, T.; Du, L.; Wang, S.; Bhunia, S. Addressing the Range Anxiety of Battery Electric Vehicles with Charging En Route. *Sci. Rep.* **2022**, *12*, 5588. [CrossRef]

7. Leng, F.; Tan, C.; Pecht, M. Effect of Temperature on the Aging Rate of Li Ion Battery Operating above Room Temperature. *Sci. Rep.* **2015**, *5*, 12967. [CrossRef]
8. Lv, S.; Wang, X.; Lu, W.; Jiaqiao, Z.; Ni, H. The Influence of Temperature on the Capacity of Lithium Ion Batteries with Different Anodes. *Energies* **2021**, *15*, 60. [CrossRef]
9. Ma, S.; Jiang, M.; Tao, P.; Song, C.; Wu, J.; Wang, J.; Deng, T.; Shang, W. Temperature Effect and Thermal Impact in Lithium-Ion Batteries: A Review. *Prog. Nat. Sci. Mater. Int.* **2018**, *28*, 653–666. [CrossRef]
10. Ouyang, D.; He, Y.; Weng, J.; Liu, J.; Chen, M.; Wang, J. Influence of Low Temperature Conditions on Lithium-Ion Batteries and the Application of an Insulation Material. *RSC Adv.* **2019**, *9*, 9053–9066. [CrossRef]
11. Wang, S.; Tang, Q.W.; Xie, H.; Li, C.; Zhang, J.; Jiang, L.; Wang, Q. Effects of Current and Ambient Temperature on Thermal Response of Lithium Ion Battery. *Batteries* **2022**, *8*, 203. [CrossRef]
12. Previati, G.; Mastinu, G.; Gobbi, M. Thermal Management of Electrified Vehicles—A Review. *Energies* **2022**, *15*, 1326. [CrossRef]
13. Sevilgen, G.; Kılıç, M.; Bayram, H.; Başak, E.; Dursun, H. The Investigation of the Multi-channel Hybrid Heat Pump System Designed and Prototyped for Heating Process of Electric Vehicles. *AEJ Alex. Eng. J.* **2023**, *68*, 417–435. [CrossRef]
14. Kök, C.; Alkaya, A. Investigation of Thermal Behavior of Lithium-Ion Batteries under Different Loads. *Eur. Mech. Sci.* **2020**, *4*, 96–102. [CrossRef]
15. Sevilgen, G.; Kiliç, M.; Aktaş, M. Dual-Separated Cooling Channel Performance Evaluation for High-Power Led Pcb in Automotive Headlight. *Case Stud. Therm. Eng.* **2021**, *25*, 100985. [CrossRef]
16. Bulut, E.; Albak, E.İ.; Sevilgen, G.; Öztürk, F. Prediction and Optimization of the Design Decisions of Liquid Cooling Systems of Battery Modules Using Artificial Neural Networks. *Int. J. Energy Res.* **2022**, *46*, 7293–7308. [CrossRef]
17. Bulut, E.; Albak, E.; Sevilgen, G.; Öztürk, F. A New Approach for Battery Thermal Management System Design Based on Grey Relational Analysis and Latin Hypercube Sampling. *Case Stud. Therm. Eng.* **2021**, *28*, 101452. [CrossRef]
18. Tran, T.-H.; Harmand, S.; Desmet, B.; Filangi, S. Experimental Investigation on the Feasibility of Heat Pipe Cooling for HEV/EV Lithium-Ion Battery. *Appl. Therm. Eng.* **2014**, *63*, 551–558. [CrossRef]
19. Ye, Y.; Saw, B.; Lip, H.; Yixiang, S.; Tay, A.A.O. Numerical Analyses on Optimizing a Heat Pipe Thermal Management System for Lithium-Ion Batteries during Fast Charging. *Appl. Therm. Eng.* **2015**, *86*, 281–291. [CrossRef]
20. Galeotti, M.; Cinà, L.; Giammanco, C.; Cordiner, S.; Di Carlo, A. Performance Analysis and SOH (State of Health) Evaluation of Lithium Polymer Batteries through Electrochemical Impedance Spectroscopy. *Energy* **2015**, *89*, 678–686. [CrossRef]
21. Chang, W.; Bommier, C.; Fair, T.; Yeung, J.; Patil, S.; Steingart, D. Understanding Adverse Effects of Temperature Shifts on Li-Ion Batteries: An Operando Acoustic Study. *J. Electrochem. Soc.* **2020**, *167*, 090503. [CrossRef]
22. Sim, S.-B.; Lee, C.-H.; Si-kuk, K. Study on the Explosion and Fire Risks of Lithium Batteries Due to High Temperature and Short Circuit Current. *Fire Sci. Eng.* **2016**, *30*, 114–122. [CrossRef]
23. Henriksen, M.; Vaagsaether, K.; Lundberg, J.; Forseth, S.; Bjerketvedt, D. Explosion Characteristics for Li-Ion Battery Electrolytes at Elevated Temperatures. *J. Hazard. Mater.* **2019**, *371*, 1–7. [CrossRef] [PubMed]
24. Rao, Z.; Qian, Z.; Kuang, Y.; Li, Y. Thermal Performance of Liquid Cooling Based Thermal Management System for Cylindrical Lithium-Ion Battery Module with Variable Contact Surface. *Appl. Therm. Eng.* **2017**, *123*, 1514–1522. [CrossRef]
25. Dan, D.; Zhao, Y.; Wei, M.; Wang, X. Review of Thermal Management Technology for Electric Vehicles. *Energies* **2023**, *16*, 4693. [CrossRef]
26. Wang, T.; Tseng, K.J.; Zhao, J.; Wei, Z. Thermal investigation of lithium-ion battery module with different cell arrangement structures and forced air-cooling strategies. *Appl. Energy* **2014**, *134*, 229–238. [CrossRef]
27. Chen, K.-H.; Han, T.; Khalighi, B.; Klaus, P. Air Cooling Concepts for Li-Ion Battery Pack in Cell Level. In Proceedings of the ASME 2017 Heat Transfer Summer Conference, Volume 1: Aerospace Heat Transfer; Computational Heat Transfer; Education; Environmental Heat Transfer; Fire and Combustion Systems; Gas Turbine Heat Transfer; Heat Transfer in Electronic Equipment; Heat Transfer in Energy Systems, Bellevue, DC, USA, 9–12 July 2017. [CrossRef]
28. Gungor, S. Analytical and Numerical Investigations on Optimal Cell Spacing for Air-Cooled Energy Storage Systems. *Int. J. Therm. Sci.* **2023**, *191*, 108332. [CrossRef]
29. Hasan, H.A.; Togun, H.; Abed, A.M.; Biswas, N.; Mohammed, H.I. Thermal Performance Assessment for an Array of Cylindrical Lithium-Ion Battery Cells Using an Air-Cooling System. *Appl. Energy* **2023**, *346*, 121354. [CrossRef]
30. Saechan, P.; Dhuchakallaya, I. Numerical Study on the Air-Cooled Thermal Management of Lithium-Ion Battery Pack for Electrical Vehicles. *Energy Rep.* **2022**, *8*, 1264–1270. [CrossRef]
31. Kummitha, O.R. Thermal Cooling of Li-Ion Cylindrical Cells Battery Module with Baffles Arrangement for Airflow Cooling Numerical Analysis. *J. Energy Storage* **2023**, *59*, 106474. [CrossRef]
32. Mei, N.; Xu, X.; Li, R. Heat Dissipation Analysis on the Liquid Cooling System Coupled with a Flat Heat Pipe of a Lithium-Ion Battery. *ACS Omega* **2020**, *5*, 17431–17444. [CrossRef]
33. Saw, L.H.; Tay, A.A.O.; Zhang, L.W. Thermal management of lithium-ion battery pack with liquid cooling. In Proceedings of the 2015 31st Thermal Measurement, Modeling & Management Symposium (SEMI-THERM), San Jose, CA, USA, 15–19 March 2015; pp. 298–302. [CrossRef]
34. Peng, W.; Xu, H.; Xu, X.; Pan, C. Design and Simulation of Liquid Cooled System for Power Battery of PHEV. *IOP Conf. Ser. Mater. Sci. Eng.* **2017**, *231*, 012025. [CrossRef]

35. Kılıç, M.; Gamsız, S.; Alınca, Z.N. Comparative Evaluation and Multi-Objective Optimization of Cold Plate Designed for the Lithium-Ion Battery Pack of an Electrical Pickup by Using Taguchi–Grey Relational Analysis. *Sustainability* **2023**, *15*, 12391. [CrossRef]
36. Rao, Z.; Wang, S.; Zhang, G. Simulation and Experiment of Thermal Energy Management with Phase Change Material for Ageing LiFePO 4 Power Battery. *Energy Convers. Manag.* **2011**, *52*, 3408–3414. [CrossRef]
37. Aslan, E.; Aydın, Y.; Ya¸sa, Y. Consideration of Graphene Material in PCM with Aluminum Fin Structure for Improving the Battery Cooling Performance. *Int. J. Energy Res.* **2022**, *46*, 10758–10769. [CrossRef]
38. Joula, M.; Dilibal, S.; Mafratoglu, G.; Danquah, J.O.; Alipour, M. Hybrid Battery Thermal Management System with NiTi SMA and Phase Change Material (PCM) for Li-Ion Batteries. *Energies* **2022**, *15*, 4403. [CrossRef]
39. Chen, J.; Kang, S.; Jiaqiang, E.; Huang, Z.; Wei, K.; Zhang, B.; Zhu, H.; Deng, Y.; Zhang, F.; Liao, G. Effects of Different Phase Change Material Thermal Management Strategies on the Cooling Performance of the Power Lithium Ion Batteries: A Review. *J. Power Sources* **2019**, *442*, 227228. [CrossRef]
40. Mbulu, H.; Laoonual, Y.; Wongwises, S. Experimental Study on the Thermal Performance of a Battery Thermal Management System Using Heat Pipes. *Case Stud. Therm. Eng.* **2021**, *26*, 101029. [CrossRef]
41. Lv, W.; Li, J.; Chen, M. Experimental Study on the Thermal Management Performance of a Power Battery Module with a Pulsating Heat Pipe under Different Thermal Management Strategies. *Appl. Therm. Eng.* **2023**, *227*, 120402. [CrossRef]
42. Pakrouh, R.; Hosseini, M.J.; Ranjbar, A.A.; Rahimi, M. A Novel Liquid-Based Battery Thermal Management System Coupling with Phase Change Material and Thermoelectric Cooling. *J. Energy Storage* **2023**, *64*, 107098. [CrossRef]
43. Chen, D.; Jiang, J.; Kim, G.-H.; Yang, C.; Pesaran, A. Comparison of Different Cooling Methods for Lithium Ion Battery Cells. *Appl. Therm. Eng.* **2015**, *94*, 846–854. [CrossRef]
44. Deng, Y.; Feng, C.; Jiaqiang, E.; Zhu, H.; Chen, J.; Wen, M.; Yin, H. Effects of Different Coolants and Cooling Strategies on the Cooling Performance of the Power Lithium Ion Battery System: A Review. *Appl. Therm. Eng.* **2018**, *142*, 10–29. [CrossRef]
45. Larrañaga, M.; Vertiz, G.; Fernandez Arroiabe, P.; Martinez Agirre, M.; Berasategi, J. A Novel Direct Liquid Cooling Strategy for Electric Vehicles Focused on Pouch Type Battery Cells. *Appl. Therm. Eng.* **2022**, *216*, 118869. [CrossRef]
46. Dubey, P.; Pulugundla, G.; Srouji, A.K. Direct Comparison of Immersion and Cold-Plate based Cooling for Automotive Li-Ion Battery Modules. *Energies* **2021**, *14*, 1259. [CrossRef]
47. Wang, C.; Zhang, G.; Meng, L.; Li, X.; Situ, W.; Lv, Y.; Rao, M. Liquid cooling based on thermal silica plate for battery thermal management system. *Int. J. Energy Res.* **2017**, *41*, 2468–2479. [CrossRef]
48. Yeow, K.; Teng, H.; Thelliez, M.; Tan, E. Comparative Study on Thermal Behavior of Lithium-Ion Battery Systems with Indirect Air Cooling and Indirect Liquid Cooling. In Proceedings of the ASME/ISCIE 2012 International Symposium on Flexible Automation, St. Louis, MI, USA, 18–20 June 2012; ASME: New York, NY, USA, 2012; pp. 585–591. [CrossRef]
49. Chen, M.; on-Mora, G. Accurate Electrical Battery Model Capable of Predicting Runtime and I–V Performance. *IEEE Trans. Energy Convers.* **2006**, *21*, 504–511. [CrossRef]
50. Kim, U.; Shin, C.B.; Kim, C.-S. Modeling for the Scale-up of a Lithium-Ion Polymer Battery. *J. Power Sources* **2009**, *189*, 841–846. [CrossRef]
51. Ho, T.; Chang, K.; Lee, S.; Kim, S. Transient Thermal Analysis of a Li-Ion Battery Module for Electric Cars Based on Various Cooling Fan Arrangements. *Energies* **2020**, *13*, 2387. [CrossRef]
52. Shetty, D.D.; Sulthan, M.; Zuber, M.; Badruddin, I.A.; Kini, C.R. Computational Design and Analysis of a Novel Battery Thermal Management System of a Single 26650 Li-Ion Battery Cell for Electric Vehicle Application. *J. Adv. Res. Fluid Mech. Therm. Sci.* **2022**, *93*, 61–75. [CrossRef]
53. Akbarzadeh, M.; Jaguemont, J.; Van Mierlo, J.; Berecibar, M. Experimental Analysis of a Liquid-Based Cooling System for Fast Charging of a High-Power Lithium Ion Cell. *Energy Perspect.* **2021**, *2*, 1–13.
54. Avila, A.; Lucu, M.; Garcia-Bediaga, A.; Ibarguren, U.; Gandiaga, I.; Rujas, A. Hybrid Energy Storage System Based on Li-Ion and Li-S Battery Modules and GaN-Based DC-DC Converter. *IEEE Access* **2021**, *9*, 132342–132353. [CrossRef]
55. Panchal, S.; Dincer, I.; Agelin-Chaab, M.; Fraser, R.; Fowler, M. Thermal Modeling and Validation of Temperature Distributions in a Prismatic Lithium-Ion Battery at Different Discharge Rates and Varying Boundary Conditions. *Appl. Therm. Eng.* **2016**, *96*, 190–199. [CrossRef]
56. Behi, H.; Karimi, D.; Kalogiannis, T.; He, J.; Patil, M.S.; Muller, J.D.; Haider, A.; Mierlo, J.V.; Berecibar, M. Advanced hybrid thermal management system for LTO battery module under fast charging. *Case Stud. Therm. Eng.* **2022**, *33*, 101938. [CrossRef]
57. Waag, W.; Sauer, D.U. Secondary Batteries–Lead–Acid Systems, State-of-Charge/Health. *Encycl. Electrochem. Power Sources* **2009**, 793–804. [CrossRef]
58. Zhang, F.; Xing, Z.; Wu, M. State of health estimation for Li-ion battery using characteristic voltage intervals and genetic algorithm optimized back propagation neural network. *J. Energy Storage* **2023**, *57*, 106277.
59. Moffat, R.J. Describing the uncertainties in experimental results. *Exp. Therm. Fluid Sci.* **1988**, *1*, 3–17. [CrossRef]
60. Hosen, M.S.; Pirooz, A.; Kalogiannis, T.; He, J.; Van Mierlo, J.; Berecibar, M. A Strategic Pathway from Cell to Pack-Level Battery Lifetime Model Development. *Appl. Sci.* **2022**, *12*, 4781. [CrossRef]
61. Madani, S.S.; Swierczynski, M.; Kær, S. The discharge behavior of lithium-ion batteries using the Dual-Potential Multi-Scale Multi-Dimensional (MSMD) Battery Model. In Proceedings of the 2017 Twelfth International Conference on Ecological Vehicles and Renewable Energies (EVER), Monte Carlo, Monaco, 11–13 April 2017; pp. 1–14. [CrossRef]

62. ANSYS Fluent Advanced Add-On Modules | PDF | Proton Exchange Membrane Fuel Cell | Anode. Scribd. Available online: https://www.scribd.com/document/344930548/ANSYS-Fluent-Advanced-Add-On-Modules (accessed on 15 August 2023).
63. ANSYS Fluent Theory Guide | PDF | Fluid Dynamics | Fluid Mechanics. Scribd. Available online: https://www.scribd.com/document/230104948/ANSYS-Fluent-Theory-Guide (accessed on 15 August 2023).
64. Kwon, K.; Shin, C.B.; Kang, T.; Kim, C.-S. A Two-Dimensional Modeling of a Lithium-Polymer Battery. *J. Power Sources* **2006**, *163*, 151–157. [CrossRef]
65. Paccha-Herrera, E.; Calderón-Muñoz, W.; Orchard, M.; Jaramillo Montoya, F.; Medjaher, K. Correction: Paccha-Herrera et al. Thermal Modeling Approaches for a $LiCoO_2$ Lithium-Ion Battery—A Comparative Study with Experimental Validation. *Batteries* **2020**, *6*, 40, Erratum in *Batteries* **2021**, *7*, 43. [CrossRef]
66. Xia, B.; Ye, B.; Cao, J. Polarization Voltage Characterization of Lithium-Ion Batteries Based on a Lumped Diffusion Model and Joint Parameter Estimation Algorithm. *Energies* **2022**, *15*, 1150. [CrossRef]

Disclaimer/Publisher's Note: The statements, opinions and data contained in all publications are solely those of the individual author(s) and contributor(s) and not of MDPI and/or the editor(s). MDPI and/or the editor(s) disclaim responsibility for any injury to people or property resulting from any ideas, methods, instructions or products referred to in the content.